Degradation of Styrene-Poly(ethylene oxide)-Based Block Copolymer Electrolytes at the Na and K Negative Electrode Studied by Microcalorimetry and Impedance Spectroscopy

View the article online for updates and enhancements.

Degradation of Styrene-Poly(ethylene oxide)-Based Block Copolymer Electrolytes at the Na and K Negative Electrode Studied by Microcalorimetry and Impedance Spectroscopy

Silin Xing,[1] Anna Khudyshkina,[2] Ulf-Christian Rauska,[2] Andreas J. Butzelaar,[3] Dominik Voll,[3] Patrick Theato,[3,4] Jens Tübke,[1,5] and Fabian Jeschull[2,z]

[1]*System Architecture, Helmholtz-Institute Ulm, D-89081 Ulm, Germany*
[2]*Institute for Applied Materials—Energy Storage Systems (IAM-ESS), Karlsruhe Institute of Technology (KIT), 76344 Eggenstein-Leopoldshafen, Germany*
[3]*Institute for Chemical Technology and Polymer Chemistry (ITCP), Karlsruhe Institute of Technology (KIT), 76131 Karlsruhe, Germany*
[4]*Soft Matter Synthesis Laboratory, Institute for Biological Interfaces III, D-76344 Eggenstein-Leopoldshafen, Germany*
[5]*Fraunhofer Institute for Chemical Technology (ICT), 76327 Pfinztal, Germany*

The electrode-electrolyte interface of alkali metal electrodes and solid polymer electrolytes (SPE) is challenging to access because solid electrolytes are difficult to remove without damaging the interphase region. Herein, the two non-invasive techniques isothermal microcalorimetry (IMC) and electrochemical impedance spectroscopy (EIS) are combined to explored degradation processes of reactive sodium and potassium metal electrodes in contact with SPEs. Comparison of the parasitic heat flows and interfacial resistances at different current densities with a liquid electrolyte (LE) system showed marked differences in aging behaviour. The data also suggest that the electrochemically active surface area of alkali metal electrodes increase with cycling, leading to larger parasitic heat flows and indicating morphological changes. SPE-based cells exhibit similar levels of parasitic heat flow at different current densities, which is in stark contrast to the LE cell where a strong correlation between the two is evident. The ambiguity of EIS spectra is challenging due to the overlapping time constants of the underlying electrode processes. However, equivalent circuit modelling can be used to follow trends in resistance evolution, for example to track the rapidly increasing cell impedance in K/K symmetric cells during a 48 h equilibration interval prior to cycling, which abruptly disappeared once cycling begins.

In solid-state batteries, where the electrolyte is either ceramic- or polymer-based, alkali metals are commonly used as negative electrodes.[1] The use of metal foils instead of porous intercalation/insertion type electrodes offers a path towards higher energy densities compared to conventional composite electrodes due to less dead weight and smaller electrode volume required to store the same number of charge carriers (under the assumption of a well-balanced N/P ratio).[2] Alkali metals are generally found to be highly reactive towards electrolyte components[3] and to undergo significant morphological changes,[4,5] which inevitably leads to rapid capacity decay upon recurring irreversible reactions at the negative electrode. Moreover the formation of the resulting surface layer, the solid electrolyte interphase (SEI), leads to gradually increasing cell resistances.[6,7]

By comparison, solid polymer electrolytes (SPEs) based on poly(ethylene oxide) (PEO) show high cathodic stability, even though this material class is commonly operated at elevated temperatures, i.e. above the melting point of PEO, as a result of their low room temperature ionic conductivity.[8,9] When polymer-based solid-state cells are built, it is challenging to assess the degrees of irreversible reactions originating from either the positive or negative electrode. Even the electrochemical stability window of polymer electrolytes is not clearly defined as the onset of degradation may be defined differently depending on how the stability measurement is conducted.[10,11] Studies on the SEI layer properties (its thickness and composition), for example by electron microscopy or X-ray photoelectron spectroscopy (XPS), cannot be conducted straightforwardly in solid-state cells either, since electrode and electrolyte are hard to separate once they were brought in contact, charging effects build up rapidly and preparation of sample cross-sections is also challenging with soft polymer matrices. Therefore, such experiments are rarely reported as great care during sample preparation is required to study the electrode interfaces intact in these systems.[12–15] There is only a limited number of techniques that are suitable to assess the degree of degradation in alkali metal/SPE/positive electrode setups. Among those techniques microcalorimetry and impedance spectroscopy are two possible options.

Microcalorimetry in particular is a powerful technique to monitor and analyse heat flows in real time over a broad time scale from minutes to weeks or even years. Heat flows can be deconvoluted into their different contributions and thus be used as a measure of structural or chemical changes in a closed system, like a coin cell. Specifically, in battery research contributions from overpotentials, irreversible reactions and structural changes at the electrodes are of interest. In this study, we leveraged the high precision in isothermal microcalorimetry (IMC) experiments to investigate the stability of a polystyrene-poly(ethylene oxide)-based block copolymer electrolyte (BPE) that was previously studied in Li-, Na- and K-metal batteries.[16] The suitability of such characterization techniques has been well-proven for several battery material investigations.[17,18] As a non-destructive analysis method, a calorimeter, which measures heat flow of steady state experiments, is here coupled with a potentiostat.[19] Moreover, employing IMC allows scientist to determine the parasitic heat generated from decomposition reactions inside the battery cell. Therefore, this also allows to compare the stability of different electrolyte compositions.[20–22]

The experiments are complemented by electrochemical impedance spectroscopy (EIS) to track changes at the alkali metal interfaces. The main challenge is to find a suitable equivalent circuit model that carries physical meaning. To this end, the Gaberšček group recently approached the problem in great detail for Li-metal electrodes in a series of studies by using generalized, physics-based transmission line models (TLMs).[23–25] The studies highlight that

especially the low frequency region gives rise to deviations with regular circuit elements, such as the Warburg impedance, as cation and anion diffusion have to be treated separately for detailed analysis.[25] Furthermore, the electrode-electrolyte interface may comprise of several porous layers, such as an outer, dead" layer that contains electrochemically inaccessible Li and an inner layer that is in electronic contact with the Li foil and the current collector.[24,26] However, this level of detail is very challenging to obtain from, regular" circuit models, as will be further discussed below.

Herein, we aim to follow up on previous works[16,27] that showed that the capacity retention of polymer electrolyte-based solid state cells comprising sodium or potassium metal as negative electrodes and a Prussian white positive electrode ($A_2Fe[Fe(CN)_6]$, A = Na, K) performed better than corresponding liquid electrolyte setups, despite higher operation temperatures. In an attempt towards understanding the contributions to the irreversible losses on both negative and positive electrodes, experiments with IMC are conducted on symmetric Na/Na and K/K cells, respectively, to assess the reactivity between the BPE-based electrolyte and the alkali metal electrodes. By comparison with a comparable liquid electrolyte system and literature data, we will demonstrate that in fact parasitic degradation processes are reduced in polymer-based solid electrolytes, although they are operated at higher temperatures.

Experimental

Electrolyte preparation and cell assembly.—Unless stated differently electrolyte preparation and cell assembly were carried out in an argon-filled glovebox (MBraun) under inert condition (H_2O < 0.1 ppm; O_2 < 0.1 ppm). All tests were conducted in coin cells (CR2032-type cells).

Solid polymer electrolyte preparation.—Synthesis and characterization of poly(vinyl benzyl methoxy poly(ethylene oxide) ether)-*block*-polystyrene copolymer (PVBmPEO-*b*-PS, denoted as BPE) were previously reported.[8] The average length of the PEO side chain was 2000 g mol^{-1}, corresponding to about 48 ethylene oxide (EO) units. The weight ratio between the PS and PVBmPEO blocks was adjusted to 50:50; the molar mass determined by size-exclusion chromatography (SEC) and ^{1}H-NMR spectroscopy was M_n = 38300 g mol^{-1}. The polymer then was dried at 80 °C under vacuum (10^{-3} mbar) for 12 h and transferred to the Ar-filled glovebox, For the electrolyte preparation bis(trifluoromethanesulfonyl)imide salts (ATFSI, where A = Na or K; 99.5%, Solvionic) and PVBmPEO-*b*-PS were mixed in a EO:ATFSI molar ratio of 15:1 (BPE$_{15}$-ATFSI$_1$) and were then dissolved in dry acetonitrile (99.8%, Sigma Aldrich). After approaching a homogeneous state of the solutions, the latter were poured into Teflon molds, followed by the solvent evaporation at 60 °C. The obtained films were dried and simultaneously annealed at 110 °C for 36 h under vacuum (10^{-3} mbar), yielding a final thickness of about ∼100 μm of the resulting solid polymer electrolytes (SPE).

Assembly of symmetric cells with SPEs.—Alkali metal electrodes were prepared from sodium metal (cubes, 99.8%, Alfa Aesar) and potassium metal (ampulla, 99.9%, Sigma-Aldrich), respectively, by rolling pieces of the materials into thin sheets, from which electrode discs were cut. Circular electrolyte films were cut from the casted materials, as described above, and sandwiched between the metallic electrodes in coin cells setup. Prior to the measurements, the cells were pre-conditioned at a temperature of 55 °C for 48 h.

Assembly of symmetric cell with liquid-based electrolytes.—Following the procedure of preparing metallic electrodes from the respective alkali metals in 2.1.2, symmetric cells with liquid electrolyte were prepared in a same manner, except that the SPE was replaced by Whatman glass fibre separators (GF/B, 16 mm). The separator was soaked with 100 μl of electrolyte comprising 0.75 M

ATFSI (A = Na, K) dissolved in ethylene carbonate:diethyl carbonate (EC:DEC = 1:1 by volume).

Isothermal microcalorimetry (IMC).—An isothermal microcalorimeter (TA Instruments, accuracy ±300 nW, temperature range from 4 to 150 °C, temperature drift over 24 h of less than ±100 μ°C) was coupled to a Biologic VSP multi-channel potentiostat, to measure the total heat flow *operando* in the liquid and solid-state electrolyte symmetric cells, respectively.

Coin cells were inserted into a custom-made cell holder connected with Cu-P-bronze wires (36AWG, Lakeshore), as shown in Figs. S1b and S1e, to reduce heat transfer between the cell and the potentiostat. The sample holder was suspended from a hook on the bottom of the lifter. The lifter in Fig. S1b consists of several thermal shields to avoid heat dissipated from the thermocouple detector. Circulating oil was used as the cooling medium to ensure a uniform and accurate temperature environment for sample measurement in isothermal mode. A schematic diagram of the calorimeter is shown in Fig. S1.

An automatic one hour of device internal calibration process was performed prior to each experiment. This process includes 15 min of resting the sample-containing ampoule at equilibrium position followed by 45 min of resting at measuring position. Afterwards, the sample chamber was gradually heated to a temperature of 55 °C until the heat flow had stabilized over the course of 48 h at OCV. In this system, the baseline drift over the time frame of measurements was lower than 5 μW. Meanwhile, the error of such setup was estimated less than ±300 nW. Galvanostatic cycling test was conducted with increasing specific current densities starting from 0.01, 0.02 to 0.05 mA cm^{-2} with ten cycles at each rate. Each cycle lasted 4 h, starting with 1 h under positive current, 1 h rest (OCV), 1 h under negative current and another 1 h rest (OCV). IMC measurements during the OCV intervals were required to determine the heat flow contributions from the electrochemical processes under applied current (see IMC and General Energy Balance Model section).

Electrochemical impedance spectroscopy (EIS).—Electrochemical impedance spectroscopy (EIS) was measured in parallel to the IMC measurements. EIS experiments were conducted under OCV conditions within the 48 h equilibration period, after the cell were transferred into the microcalorimeter, in the frequency range of 10 mHz to 200 kHz and a voltage amplitude of 20 mV. In addition, EIS was measured after each 10 cycles. The EIS data were normalized to the electrode area, as Na- and K-cells were built with different electrode diameters (the quality of the EIS data improved for K-cells when larger electrode diameters were used).

Background

IMC and general energy balance model.—Due to electrolyte stabilities as well as SEI formations, the parasitic reactions vary in different battery materials. Employing the general energy balance model enables derivation of thermodynamic data out of the heat flow signal which was recorded by IMC.[28] The simplified version of such general energy balance model was further improved by Downie et al.[20] The suitability of such model in different battery designs including the variation of different electrodes and electrolytes has been well-evaluated in former research publications.[29–34] Moreover, the suitability of employing such model for electrode-electrolyte-interphase investigation with involvement of polymer electrolytes has also been proven by Zarrabeitia et al.[19] Meanwhile, for alkali metal electrode and dendrite-free systems, such models have proven appropriate as well.[35] In an adaptation of this earlier work, the general energy balance model is employed in this study to SPE-based symmetric cells.

The mean total heat flow was evaluated by the integration of the heat flow pulse divided by the length of current pulse, as shown in the following equation:

$$\dot{Q}_{tot} = \int_0^{t_{dis}} \dot{Q}_{tot,dis}dt + \int_0^{t_{ch}} \dot{Q}_{tot,ch}dt \qquad [1]$$

where t is the discharge or charge time, $\dot{Q}_{tot}$ is the measured heat flow,[28] which can also be converted to the following:

$$\dot{Q}_{tot} = \dot{Q}_{polarization} + \dot{Q}_{parasitic} + \dot{Q}_{rev} \qquad [2]$$

where $\dot{Q}_{polarization}$ is the polarization heat flow from overpotentials and ohmic losses, $\dot{Q}_{parasitic}$ is the parasitic heat flow as the sum of all irreversible, non-Faradaic reactions, $\dot{Q}_{rev}$ is the reversible heat flow that emanates from entropy changes during the Faradaic reaction of the underlying electrochemical process.

Equation 2 can be converted into the general energy balance model (Eq. 3), developed by Bernardi et al.[28] and simplified by Downie et al.[20]

$$\dot{Q}_{tot} = I(E_{load} - E_{eq}) + \sum_i \Delta H_i r_i + IT\left(\frac{dE_{eq}}{dT}\right) \qquad [3]$$

where I is the current, E_{load} is the cell voltage under operation, E_{eq} is the equilibrium cell voltage, ΔH_i is the reaction enthalpy of a chemical side reaction occurring at a rate r_i, T is the temperature and the quotient $\frac{dE_{eq}}{dT}$ is called the entropic heat coefficient, which is related to changes in the entropy by $\Delta S = nF\left(\frac{dE_{eq}}{dT}\right)$ with the proportionality constant n and Faraday's constant F. The cumulative effect of heat flow attributed to non-Faradaic reactions is consolidated in the second term of Eq. 3, the parasitic heat flow $\dot{Q}_{parasitic}$. To better extract the heat from SEI formation, the heat of one stripping and plating cycle are considered to be the target unit of study. Following the assumption by Krause et al.,[36] the entropic heat flow equals out over a full discharge/charge cycle, therefore the amount of parasitic heat can be then calculated using the following equation:

$$Q_{parasitic} = \left[\int_0^{t_{dis}} \dot{Q}_{tot,dis}dt + \int_0^{t_{ch}} \dot{Q}_{tot,ch}dt \right]$$
$$- \left[\int_0^{t_{ch}} I_{ch}E_{load,ch}dt - \int_0^{t_{dis}} I_{dis}E_{load,dis}dt \right] \qquad [4]$$
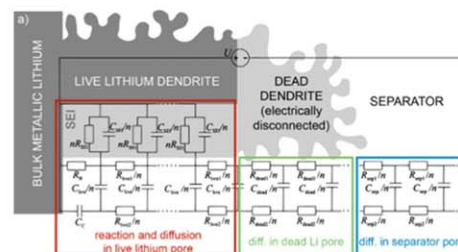
Equivalent circuit models for metallic electrodes.—Using equivalent circuit models (ECM) in EIS is the attempt to translate the response of a periodic voltage or current perturbation by an electrochemical system back into known electrical circuit components, on the basis of physically tangible parameters. Vice versa, ECM could be constructed from mathematical expressions of the underlying physico-chemical processes if those are known.[37] ECM without electrochemical considerations usually comprise of a series of Voigt elements (Fig. 1A), i.e. an arbitrary number of RC elements (resistance R and capacitor C).[38] In literature, additional elements are often added for example to express diffusion processes, which is why they have also been termed "arbitrary circuits."[23] Although such ECM yield good fitting results, the physical meaning of these parameters is undefined[39,40] as there is no dependency between RC elements. However, electrochemical processes are usually coupled, such as charge-transfer and its associated mass transport and different processes occur simultaneously and often on similar time scales. Therefore, "arbitrary ECM" provide satisfactory results whenever relaxation times of different electrode processes are well separated.

Because of the complexity and the ambiguous nature of different ECM[41] selecting "the correct equivalent circuit" for an in-depth analysis is challenging not least for occasional EIS users. Even more so when porous electrodes are investigated, for which so-called transmission line models[42,43] show the best agreement with
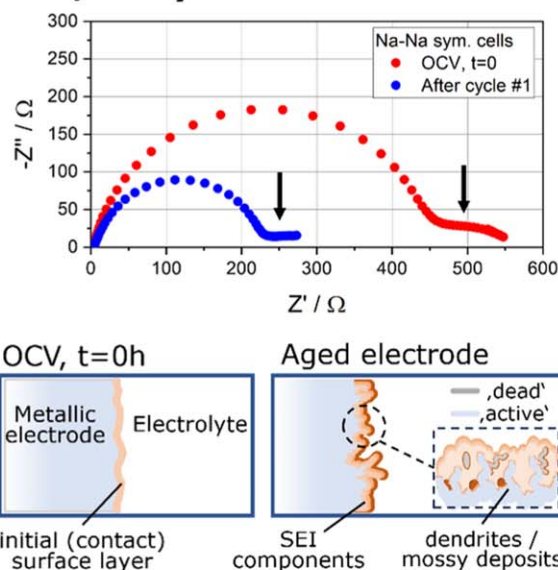

A ,arbitrary circuit' (example)
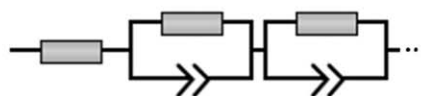
B 2D TLM (Drvarič Talian et al.)

C Na/Na symmetrical cell

OCV, t=0h — Aged electrode

D SCRF circuit model (Atebamba et al.)
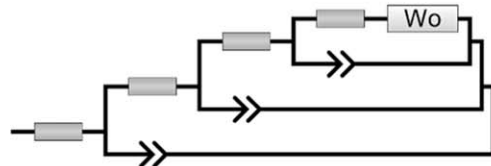
Figure 1. (A) Example of the "arbitrary circuit" (series of Voigt circuits, often with Warburg impedance), (B) 2D transmission line model (TLM) developed for metallic electrodes (B). *Reproduced under terms of the CC-BY license.*[50] *© 2019 The Authors. Published by American Chemical Society.* (C) Example of an EIS spectrum (Nyquist plot) of a Na/Na symmetric cell (liquid electrolyte) directly after assembly and after the first cycle (2-electrode setup). At OCV an initial surface layer forms due to the contact of electrolyte and the reactive metallic negative electrode. During cycling and repeated stripping and plating, mossy deposits and dendrites grow in a matrix of electrolyte degradation components (SEI components). (D) SCRF model.[51]

experimental data and that are footed on a sound physical basis. A prominent example is the Warburg impedance[44] or the Bisquet circuit[45] for diffusion in porous systems. The general semi-infinite Warburg diffusion, Z_W, generates a 45° line in Nyquist plots that is represented by an infinite length TLM comprising of resistors and

capacitors. More often than semi-infinite behaviour, finite diffusion behaviour is observed, for which the finite-length and the finite-space Warburg diffusion (FLW and FSW) can be defined, as shown in Eqs. 5 and 6.

$$Z_{FLW} = \frac{Z_W}{\sqrt{i \cdot \omega \cdot \tau}} \cdot \tanh((i \cdot \omega \cdot \tau)^\alpha) \qquad [5]$$

$$Z_{FSW} = \frac{Z_W}{\sqrt{i \cdot \omega \cdot \tau}} \cdot \cosh((i \cdot \omega \cdot \tau)^\alpha) \qquad [6]$$

Z_w is the Warburg coefficient ($\Omega \sqrt{s}$), ω is the angular frequency, τ is the time-constant (s) and α is an exponential factor (ideally 0.5). Because of their 45° line they are indistinguishable at high frequencies from the semi-infinite Warburg diffusion. At low frequencies Z_{FSW} respond with a capacitive like behaviour (blocking or reflective boundary condition) that is commonly observed in storage materials. Z_{FLW} develop a semicircle-like arc representing the finite diffusion for instance through a layer or pore (transmissive boundary conditions). The TLM in this case is terminated by either a resistor (FLW) or a capacitor (FSW).[44]

TLM that also take electrode processes into consideration rapidly reach a complexity that goes beyond what regular EIS analysis software can handle (e.g. many cross-dependencies that run quickly in a local minimum during fitting). The Gaberšček group,[24–26] pointed out that the quality of the models improves considerably when 2D or 3D TLM are used even in allegedly simple systems of (initially) non-porous symmetric Li/Li cells with liquid electrolyte (Fig. 1B). For instance, the Warburg impedance assumes that the resistance in one rail of the transmission line is negligibly small, which simplifies the mathematical description significantly.[46] This leaves one rail for ion transport and thus assumes similar ion transport properties for both the positive and negative charge carrier (in a salt A^+X^-). Especially for polymer electrolytes this is unlikely the case, as the transference numbers of cationic and anions species, here A^+ (A = Li, Na, K) and the TFSI-anion, are quite asymmetric and high degrees of ion-pairing is expected.[47,48] In addition, the cation crosses the electrode interface as it is involved in the redox reaction at the electrode (charge-transfer resistance), while the anion does not and instead participates in the formation of the double layer (double layer capacitance).[25] Under such "unsupported" conditions (Macdonald[41]) more general solutions of the Poisson-Nernst-Planck equations are required.[49] The 2D and 3D TLM developed by Moškon et al.[24] account for different diffusion resistances and also the fact that the "active ion" (e.g. Li-ion) undergoes a charge-transfer reaction, while the anion contributes to charging the double layer (including a leaking current in case of decomposition). Because in porous system there are typically several electrode processes in parallel and due to the co-dependency of charge-transfer and mass transport, additional low-frequency arcs lead to elongated low-frequency tails, as the ones observed in Na/Na symmetric cells (liquid electrolyte) shown in Fig. 1C.

During cycling the surface roughness increases and causes recurrent electrode degradation reactions. The aforementioned low-frequency tails are challenging to simulate adequately with conventional ECMs, except in the case of the "arbitrary circuit" which could simply add a larger number of Voigt elements in series, corresponding to many small semicircles in this region. For the case of Li electrodes (in a LiTFSI-glyme electrolyte) Drvarič Talian et al. explained the changes in EIS spectra by the surface coverage of dendritic and mossy structures on the Li surface (Fig. 1D) and develop a 2D TLM model that was solved by the mesh current method.[50] The creation of new surface area at the electrode leads overall to a decrease in the cell impedance, despite the significant growth of SEI on the electrode.

Between these advanced approaches and "arbitrary circuits" there are possibilities to use simplified TLM, in which TLM are reduced back into more easy-to-use equivalent circuits, such as the "SCR"

and "SCRF circuit" model reported by Atebamba et al.[51] The authors used this nested circuit to account for particle-to-particle wiring, contact resistances at the electrode-current collector interface and surface layers at the electrode interface of porous electrodes. While contact resistances are minor or no problems in metallic electrodes with stripping/plating reactions, porous electrode surfaces are expected to evolve as the electrode ages with cycling,[52] which is associated with recurrent irreversible reactions and thus SEI formation and growth. In the particular case of solid electrolytes, electrolyte resistance coupled to geometric (dielectric) capacitance also needs to be taken into consideration. Incidentally, these types of nested circuits are also found in corrosion science[53] to describe porous passivating layers. In a recent study on non-linearity of the SEI overpotential in symmetric A/A cells (A = Li, Na, K) Hess[54] used an equivalent circuit comprising four nested RQ elements of which two were required to fit the main arc and another two to fit the low frequency region. In the sections below, we will further outline our motivation to modify the model in the context of this work.

Results and Discussion

The cathodic stability of the block-copolymer-based electrolytes at the Na- and K-metal interface was tested in symmetric cells using IMC and impedance spectroscopy and thus fully focus on the stability at the polymer/alkali metal interface and to exclude heat flow contributions in the IMC measurements from oxidative degradation at the positive electrode. Similarly, impedance spectroscopy results are easier to interpret in a symmetric cell setup with flat metallic electrodes (as compared to porous electrode composites) in absences of suitable reference electrodes. Both techniques were applied in a single experiment at elevated temperatures (55 °C) using Na/Na and K/K symmetric cells with a block-copolymer PVBmPEO-*b*-PS[8,16] solid polymer electrolyte with ATFSI (A = Na, K) conducting salt (EO:A molar ratio 15:1; referred to as "BPE" in the following). For comparison, data was acquired for symmetric cells operated in liquid electrolyte formulations at the same temperature for the Na/Na configuration. The corresponding K/K configuration could not be cycled in liquid electrolyte at 55 °C.

Heat flow of BPE-based electrolytes in Na/Na and K/K symmetric cells.—The polymer electrolyte cells were equilibrated under OCV condition at 55 °C for 48 h before cycling processes started. The cells were subjected to a small rate test in which the current density was increased from $10 \, \mu A \, cm^{-2}$ to $50 \, \mu A \, cm^{-2}$. At each rate a sequence of 10 stripping-plating cycles was performed and after each rate an impedance spectrum was recorded to track the changes at the electrode-electrolyte interface.

The voltage profiles and corresponding heat profiles for the BPE-based electrolyte symmetric cells for both the sodium and potassium system are shown in Fig. 2.

Voltage profile characteristics.—The voltage profiles for the Na/Na and K/K symmetric cells are shown in Fig. 2A **(middle).** The voltage transients are consistent with the ones reported in previous work for Na-BPE and K-BPE.[16] Despite the fact that the operation temperature was chosen above the melting point of the PEO-phase in the block copolymer (the second, polystyrene, block is fully amorphous and shows merely a glass transition temperature around 100 °C[8,27]), the overpotentials quickly reached values of several hundred mV at comparatively small current densities.

Both SPE cells displayed significantly higher polarization overpotentials of initially around 180 (Na/Na) and 380 (K/K) mV, respectively, as compared to a corresponding liquid electrolyte Na/Na cell (around 10 mV) at the lowest current density of $10 \, \mu A \, cm^{-2}$. During the sequence the voltage gradually increased with each cycle. Even though in symmetric cell, stripping and plating happen at the same time on metallic electrodes, but it is still worth mentioning that, in a single stripping step, the polarization increases further over the course of the stripping process, resulting in steadily increasing
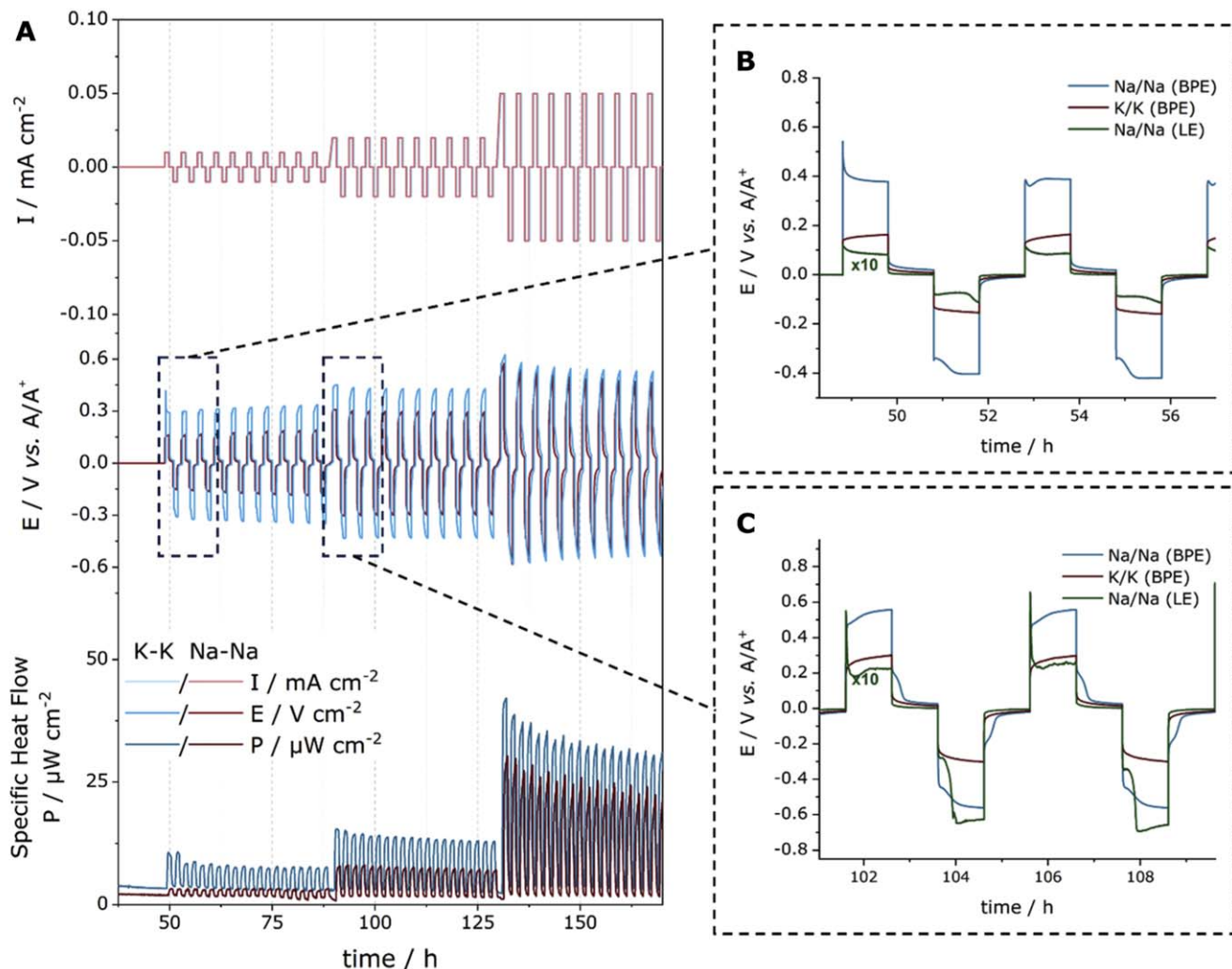
Figure 2. (A) IMC measurements: applied current density (top), cell voltage (middle) and total heat flow (bottom) of BPE-based Na/Na (red, solid) and K/K (blue, solid) symmetric cells; Zoomed voltage profiles during b) sequence 1 (B) and sequence 2 (C). The voltage profile of the liquid electrolyte cell was enlarged 10-fold.

voltage profiles. A similar behaviour was observed in the opposite direction during plating. In addition, in the voltage profiles of the K/K cell at the lowest current density, a voltage spike or peak was observed likely related to initial kinetic barriers for deposition or dissolution of metallic potassium. Similar features were described previously in literature[55,56] for liquid electrolytes as well. For liquid electrolyte systems spike-like features, especially after a current step, are usually ascribed to different stages of nucleation and growth of alkali metals during the deposition process.[57] Such spikes were clearly visible during Na-stripping as shown in Figs. 2B & 2C, for the voltage profiles of the liquid electrolyte Na/Na cell. In contrast, during plating there was a plateau-like feature at lower overpotentials first, before the voltage transient increased further in a step-like manner.

Interesting is also the behaviour during the 1 h rest between the positive and negative current step. When the current flow stops the IR drop leads to a voltage drop for the liquid electrolyte cell from 8 mV to 3 mV, and for the BPE cells from 162 mV to 57 mV (Na/Na) and from 377 mV to 162 mV (K/K), respectively. The values given provide a rough view of the magnitude of the potential drop, as the extracted absolute values strongly depend on the probing rate in the first hundred milliseconds to seconds of the experiment. The IR drop is followed by an exponential voltage decay that proceeds rapidly for LE systems and approaches value between 1–2 mV within 15–20 min (Figs. 2B & 2C) when the lowest current density is

applied. For 20 μA cm^{-2} and 50 μA cm^{-2} the relaxation lasted 15 min and 30 min longer, respectively. In contrast, the voltage relaxation for BPE systems only approached stable values towards the end of the OCV intervals. Interestingly, in K/K cells the voltage relaxation was significantly delayed at 20 μA cm^{-2} and 50 μA cm^{-2} by an unknown process that prevented the cell from entering an exponential voltage decay. Hence, it is worth to highlight that there are notable differences between the three systems not only with regards to liquid and solid electrolytes, but also regarding the impact of different alkali metals as electrodes.

The voltage transients can be further understood as a super-position of overpotentials from different electrochemical processes. On the basis of the Doyle-Fuller-Newman (DFN) model it can be shown that charge transfer overpotentials tend to exhibit a voltage peak at the beginning of the current pulse, while steadily increasing voltage transients indicate electrolyte mass transport overpotentials.[58,59] The third type, the solid diffusion overpotential, is expected to be small in comparison to the other two types, due to the use of metallic electrodes. Moreover, diffusion through the SEI layer at the electrode-electrolyte interface may present an additional parameter that comes into play, particularly with increasing dete-rioration of the metallic electrodes.[50]

For SPE a considerable contribution to the total overpotential is their low ionic conductivity compared to liquid electrolytes. As demonstrated in our previous work,[16] the ionic conductivity itself is

only part of the issue, since significantly smaller values were observed in a corresponding Li-Li system. For example, Hess[54] attributed higher non-linear SEI overpotentials to K/K symmetric cells (LE) than corresponding Na/Na or Li/Li cells. It is well known that the reactivity of Na and K towards electrolyte components is significantly increased.[60] As a result, the SEI layer can represent a larger obstacle for ions to cross the interphase, especially if the SEI layer grows thicker than on a Li surface. This, however, is very challenging to show in SPE-based batteries, since removal of the electrolyte phase the way it is commonly done for liquid electrolytes typically leads to destruction of the electrode-electrolyte interface.[61] At the same time preparation of cross-sections for instance by sputter techniques can readily induce irreversible changes.

Heat flow analysis.—Although calorimetry cannot reveal changes in the surface composition by itself, it is a sensitive measure of the degree of irreversible degradation processes during storage and cycling of a cell. In the following, the heat profiles of Na/Na and K/K symmetric cells are discussed for the respective solid BPE-based electrolytes and an EC:DEC-based liquid electrolyte mixture. The analysis includes heat profiles during OCV phases before cycling and in between cycling sequences, which were also used to acquire EIS spectra, as well as heat profiles for the stripping/plating processes at different current densities.

OCV condition.—After the assembly process, the cells were transferred into the IMC with a stably controlled temperature of 55 °C and stabilized for 48 h. The heat profiles for the last 3 h of the OCV conditioning are shown in Figs. S2a & S2b. For easier comparison the average heat flows during this acquisition period are reported in Fig. 3. At the end of this OCV period, the cells with EC:DEC-based liquid electrolyte exhibit a heat flow of around 1.5 μW cm^{-2} (Na/Na) and 3 μW cm^{-2} (K/K), which are slightly lower heat flow offsets, by about 0.5 μW cm^{-2}, than for corresponding symmetric cells with the solid Na- and K-BPE electrolytes, respectively. This slightly unexpected result means that in contact with the respective raw alkali metals and before any cycling process, the EC:DEC-based liquid electrolytes were found to undergo smaller degrees of reaction than polymer-electrolyte containing cells.

Heat flow during OCV sections between cycling sequences.—Between cycling sequences at different current densities an OCV phase was added to measure EIS, in parallel to the ongoing heat flow measurement. The heat flow offsets for both the EC:DEC-based LEs and the BPE symmetric cells are provided in Figs. S2c–S2h; and the average heat flows are included in Fig. 3. From the comparison it can be readily seen that the heat flow of the liquid electrolyte cells kept increasing notably as cycling progressed, reaching over 8.64 μW cm^{-2} for K/K symmetric cell and 7.59 μW cm^{-2} for the Na/Na symmetric cell. In contrast, the heat flow offset remained relatively constant for BPE-cells throughout the cycling process, with an average increase from 1st to 30th cycle of <0.6 μW cm^{-2} for the K/K cells and <0.2 μW cm^{-2} for Na/Na cells. Already after the first 10 cycles with current density of 10 μA cm^{-2}, the heat flow offset of cell with EC:DEC-based liquid electrolyte became higher than the offset of cell containing BPE-based solid electrolyte. This means that with onset of the charging/discharging process at the electrodes, i.e. Na or K stripping and plating, the surface was activated such that the degree of degradation processes increases considerably in EC:DEC-based LEs against metallic electrodes. The results will be further discussed below also in the context of the interfacial impedance from EIS measurements.

Heat flow during cell cycling.—In Fig. 2A **(bottom)**, it was observed that the heat flow of the K/K symmetric cell with PVBmPEO-*b*-PS-based electrolyte was higher than that of the Na/Na symmetric cell during charge and discharge processes. The results of a detailed heat flow analysis (IMC and General Energy Balance Mode section) on the parasitic (Q$_{parasitic}$) and polarization
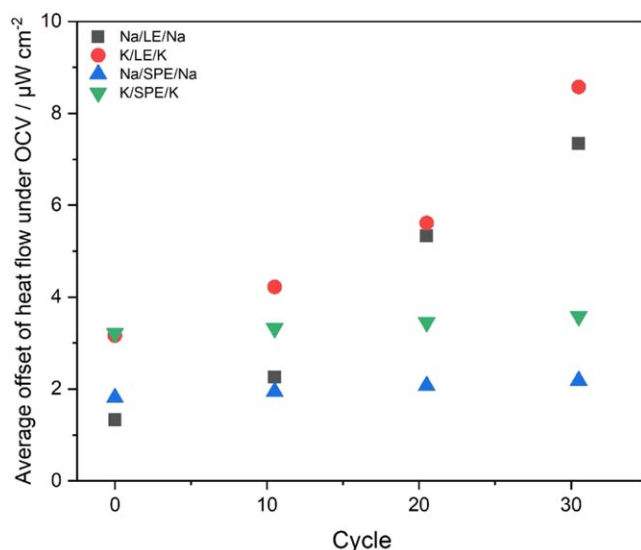

Figure 3. Comparison of average offset in heat flow profile for all 4 different cells under different OCV period.

(Q$_{polarization}$) contributions to the total heat flow (Q$_{tot}$) in Na/BPE/Na and K/BPE/K symmetric cells, as well as for a Na/LE/Na cell, is shown in Fig. 4. In case of solid electrolytes, a high contribution of the polarization resistance can be explained by the comparatively low ionic conductivity, especially in terms of cation transference number T$_+$. At 55 °C the ionic conductivity of BPE-based electrolytes is in the range of $5\cdot10^{-4}$ S cm^{-1} for both the Na- and K-SPE,[16] while EC:DEC-based electrolyte formulations show room temperature ionic conductivities in the range of 10^{-3} S cm^{-1}, depending on the type of electrolyte salt used. Transport of charge carriers in SPEs is therefore usually associated with a higher mass transport resistance than in conventional liquid electrolytes. For this reason, Q$_{polarization}$ increases significantly with increasing current density over the three cycling sequences. Q$_{parasitic}$ is larger in K/K than in Na/Na symmetric cells (Figs. 4a & 4b), which generally agrees with the relative order of reactivities amongst alkali metals (Li < Na < K). The parasitic heat flow due to irreversible reactions in the Na/Na cell is about half that of the K/K cell (Table I). Interestingly, the heat flow stays within the same margin (24.6 ± 4.0 mJ cm^{-2} (Na) and 49.6 ± 3.0 mJ cm^{-2} (K)), but shows generally higher parasitic heat flow in the first cycles of a new cycling sequence. Because of the increase in Q$_{polarization}$ with increasing current densities, the relative contribution of Q$_{parasitic}$ (in %) to Q$_{tot}$ decreases (Table I).

In contrast, in the Na/Na LE symmetric cell Q$_{polarization}$ is comparatively small to the solid electrolyte systems and Q$_{parasitic}$ is the dominant contributor to Q$_{tot}$. A major difference is the strong correlation between parasitic heat flow and applied current density (Table I, Fig. 4c). At 20 μA cm^{-2} similar values were obtained for Q$_{parasitic}$ in LE and SPE Na/Na cells, whereas at 50 μA cm^{-2} Q$_{parasitic}$ of the LE-based cell even exceeds the values measured for the SPE-based cell. Unfortunately a detailed heat flow analysis of the K/LE/K symmetric cell was not possible and thus excluded from this comparison due to drifting heat flow readings, indicating significant chemical changes under the tested conditions at 55 °C (Fig. S4a).

Electrochemical impedance spectroscopy (EIS).— *Equivalent circuit model for symmetric alkali metal-SPE cells.*—Figures 5A & 5B show the Nyquist and Bode representation of the spectrum recorded after the first cycling sequence at 10 μA cm^{-2} and the corresponding simulated equivalent circuit model that is suggested in Fig. 5D. The ECM is based on a nested circuit model, such as the one proposed by Hess.[54] The circuit elements R1 and C1 are ascribed to the geometric capacitance of the polymer electrolyte,[62]

A Na/BPE/Na
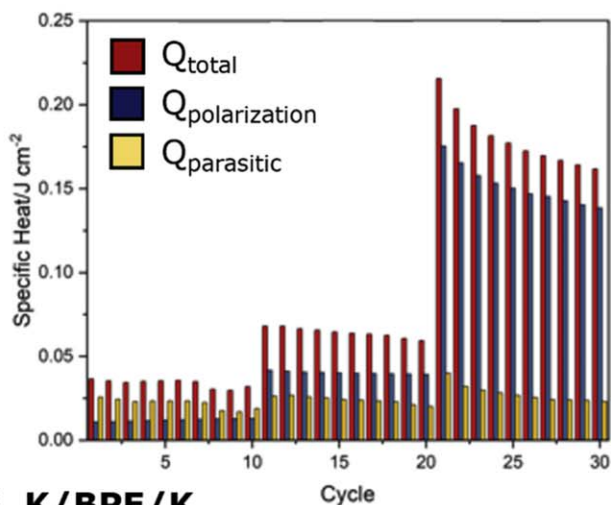
B K/BPE/K
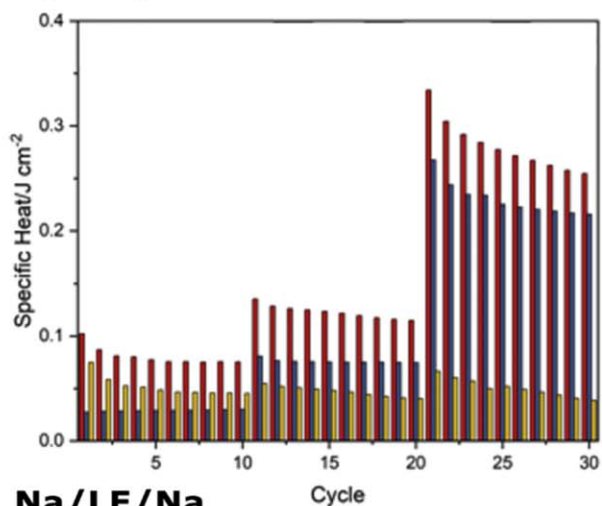
C Na/LE/Na
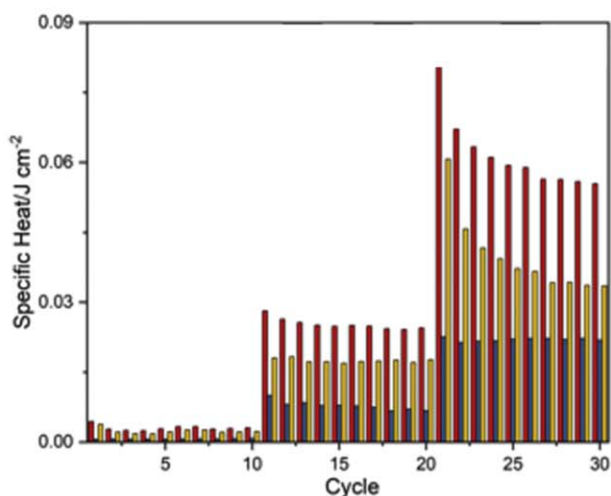
Figure 4. Heat separation of sodium symmetric cell (A) and potassium symmetric cell (B) with polymer electrolyte, sodium symmetric cell (C) with liquid electrolyte of 30 cycles employing current densities from 0.01, 0.02 to 0.05 mA cm^{-2} during each 10 cycles.

that manifest themselves as incomplete semicircle. As shown in the inset of Fig. 5A only the last section of the semicircle can be seen, the capacitance is several orders of magnitude lower than what is

expected for a double layer or SEI layer (here in the order of 10^{-10} F). The next inner circuit of R2 and Q1 (constant phase element, CPE) are ascribed to a surface film on the electrode, i.e. the SEI layer. The innermost circuit consists of a Randles-type circuit with a CPE for the double layer capacitance Q1, a charge-transfer resistance R2 in series with the two finite diffusion Warburg elements, Z_{FSW} ("open" Warburg, W_o) and Z_{FLW} ("short" Warburg, W_S; see Equivalent circuit models for metallic electrodes section). For more clarity regarding the contribution of each RC couple in the nested configuration, their isolated frequency response was added in the Nyquist plot in Fig. 5A. The resulting circuit model in Fig. 5D resembles that of the simplified contact-Randles film (SCRF) circuit derived by Atebamba et al.[51] from general transmission line model considerations on porous electrodes. Although there seems little overlap of the two systems (porous composite electrode vs flat metallic electrode), it was demonstrated more recently that the evolving electrode porosity at the alkali metal electrode/electrolyte interface changes the EIS response profoundly[50] (Fig. 5C).

The number of elements was derived empirically starting from the minimum number of elements necessary (including removal of R2 and Q1). However, it turned out that Z_{FLW} (diffusion in porous matrix or across the interface) was not sufficient to account for the low-frequency tail in the spectra. Therefore, the charge-transfer process was also coupled to Z_{FSW}, that can be interpreted as a concentration gradient in the electrolyte that builds up at low-frequencies due to slow cation transport in the electrolyte, as previously suggested by Kitz et al.[63] As the interface becomes more depleted with electroactive species under these conditions the resistance increases, and other effects are rendered less relevant. As can be seen in the profile of the simulated circuit at low frequencies in the Nyquist plot (Fig. 5A), the model generates a wave-like tail which does not fit in all cases perfectly to the spectra. For the fitting, Nyquist plots were not sufficient to evaluate the quality of the fit. Simulated profile also needed to match the Bode plots for |Z| and phase angle (Fig. 5B). There is clearly a risk of overparameterization in this model, especially considering three variables per Warburg element. Some degrees of freedom had to be restricted, like the alpha values that control deviation from the 45° slope, in order to avoid the simulation to drift off. Similarly, the n-value for the CPE was restricted to a lower limit of 0.8.

EIS of solid-electrolyte cells (OCV after 48 h, prior to cycling).— After equilibration in the IMC at OCV at 55 °C for 48 h, EIS spectra were recorded prior to the cycling sequences for both Na/BPE/Na and K/BPE/K cells. The spectra and their corresponding simulated circuits are shown in Fig. 6. The EIS spectra of the two types of cells show obvious differences in their shapes and magnitudes. The surface-normalized (geometric factor) absolute impedance |Z| at 1 Hz is larger by a factor of 10 for the K/BPE/K cell (99 064 Ω cm^2), as compared to the Na/BPE/Na cell (10 173 Ω cm^2). The frequency indicators in Fig. 6 show that the arcs of the two cells are shifted considerably in the frequency domain, as the maximum value in case of the Na/BPE/Na cell is reached at around 100 Hz, while for the K/BPE/K cell the relaxation frequency is two orders of magnitude lower. Analysis based on the ECM suggested in Fig. 5D was carried out and the fitting parameters for the three resistors and the two Warburg coefficients are included in Figs. 7A–7D; other fitting parameters (capacitances, alpha exponent and Warburg time constant) are provided in the *Supporting Information* (Fig. S7). Each measurement was labelled with a sample index, which correlates with acquisition time (indices 1–2: OCV spectra, indices 3–8: spectra in the OCV phase between cycling sequences). Forward and backward scans of each measurement were separated in Fig. 7, as (minor) time dependent changes were observed. The sample index thus comes in pairs, but the fitting results are slightly different in most cases due to time variance.

The resistance R1 for the solid electrolyte remains nearly constant in all samples. C1 is in the expected range of 10^{-10} F cm^{-2} for geometric capacitance. The high- and

Table I. Summary of the parasitic heat flow for a liquid electrolyte (LE) Na/Na symmetric cell and the SPE-based Na/Na and K/K symmetric cell configurations. The absolute parasitic heat (abs. $Q_{parasitic}$) is given in mJ cm^{-2} and the relative parasitic heat (rel. $Q_{parasitic}$) of each cycling sequence is $Q_{parasitic}/Q_{tot}$ ratio (in %). The values were averaged over all 10 cycles of a sequence.

| Cell configuration Current density	Na/LE/Na[a]	Na/BPE/Na[b]	K/BPE/K[b]
	abs. $Q_{parasitic}$/mJ cm^{-2} (rel. $Q_{parasitic}$ /%)		
10 μA cm^{-2}	2.3 (76.6%)	21.9 (64.4%)	51.5 (63.7%)
20 μA cm^{-2}	17.5 (69.3%)	24.0 (37.3%)	46.9 (38.1%)
50 μA cm^{-2}	39.7 (63.9%)	27.8 (15.4%)	50.5 (17.9%)

a) LE: 750 mM NaTFSI in EC:DEC (v/v = 1:1) b) BPE: PVBmPEO-b-PS:ATFSI (A = Na, K), EO:A$^+$ = 15:1

midfrequency range is dominated by R2 and Q1. The transition into the tail-like feature and the local impedance minimum at low-frequencies can be simulated relatively accurate by the combination of R3 and Z_{FLW}. Z_{FSW} is critical for the onset of second arc as the impedance increases again. However, "stretched" tails, like the one in Fig. 6A, are difficult to simulate without producing a "wave-like" tailing that are a result of Z_{FLW} that drops back to the Z' axis, while Z_{FSW} moves into the opposite direction. For a more accurate description, more sophisticated models would be needed. The parameters of Z_{FSW} are associated with a comparatively high

uncertainty as more data at lower frequencies would be needed to improve the quality of the simulation.

Interestingly, for K-cells, the magnitude of Z_{FSW} barely plays any role in the frequency range studied (Fig. 7D). The semicircle at high- and mid-frequencies formed by R2 and Q1 shows a smaller slope towards low-frequencies, which is a sign for larger values of R3 and Z_{FLW}, as indicated in Figs. 7C and 7D. At the end of the equilibration phase, cell impedances were found about 30-times as large as than for corresponding Na-cells. Again, fitting the low-frequency tail is challenging but provides satisfactory results. As there were no local minima observed in the studied frequency range, Z_{FSW} contributes a comparatively small fraction to the overall impedance. In K/BPE/K cells, the resistances R2, R3 and Z_{FLW} showed a strong dependence on the OCV storage time, which was observed during regular EIS measurements during the 48 h equilibration phase (intervals of about 3.5 h, including the EIS measurement). The evolution of the fitting parameters and Nyquist plots of selected spectra are shown in Figs. S8 and S9. The continuous increase is readily seen when studying the resistance parameters R2 and R3 that increase from the first measurement (index 1) to the last measurement (index 14) from 18 545 Ω cm^2 to 108 936 Ω cm^2 (R2) and 3 217 Ω cm^2 to 40 661 Ω cm^2 (R3), respectively.

The absolute heat flows for K-cells than for Na-cells ($\sim$3.0 μW cm^{-2} as compared to $\sim$1.7 μW cm^{-2}, Fig. 3) suggested higher degrees of parasitic processes in the K/BPE/K cell, which in general agreement with larger values for R2, the surface layer resistance. The growth of R2 in the K-cell, however, is
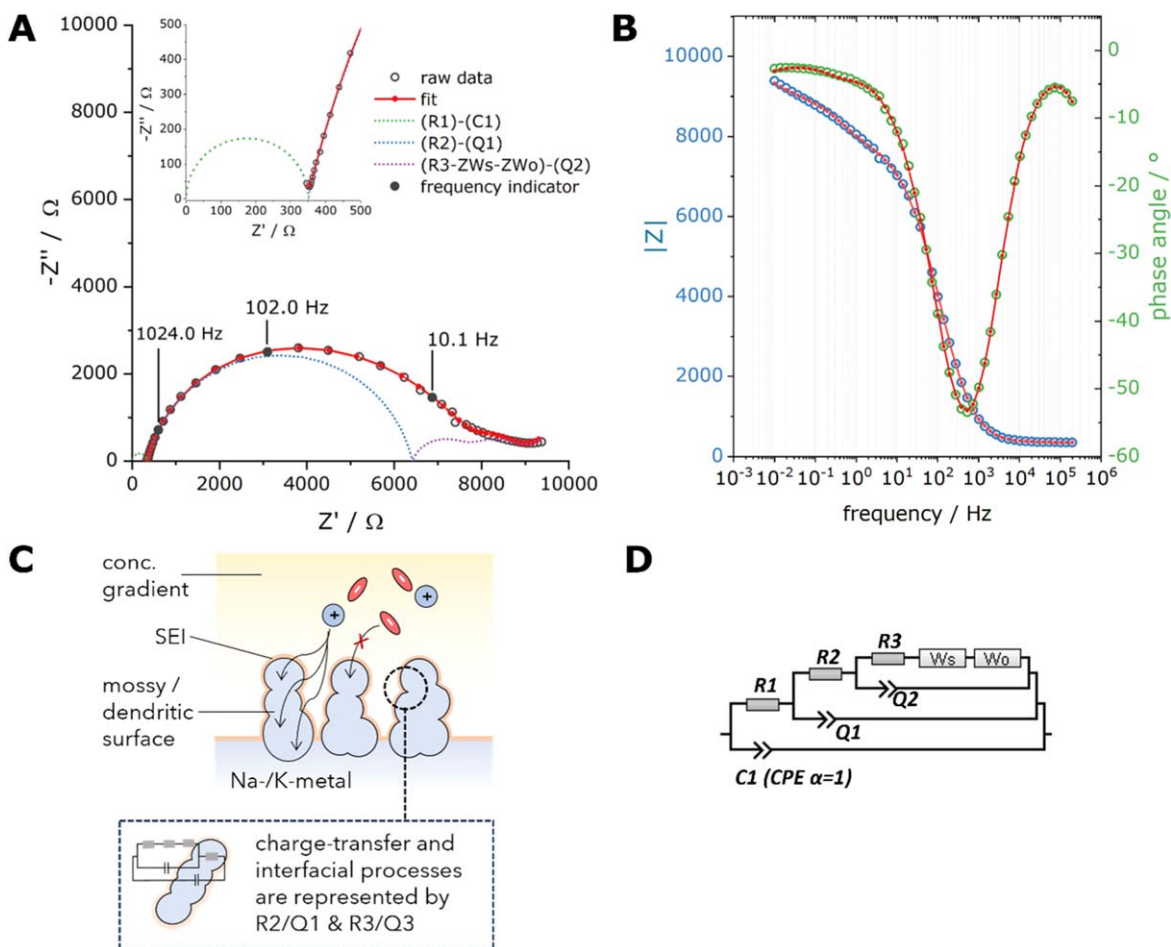
Figure 5. Analysis of the intermittent EIS analysis during OCV conditioning and cycling sequences with increasing current densities at an operating temperature of 55 °C. (A) Nyquist plot of the EIS spectrum, after the first cycling sequence (inset of the high frequency region). (B) Corresponding Bode representation of the data in A for the absolute impedance |Z| and the phase angle and corresponding simulated results. (C) Schematic of surface processes at alkali metal electrodes with mossy (porous) structures. (D) Suggested equivalent circuit and illustration of the electrode processes.
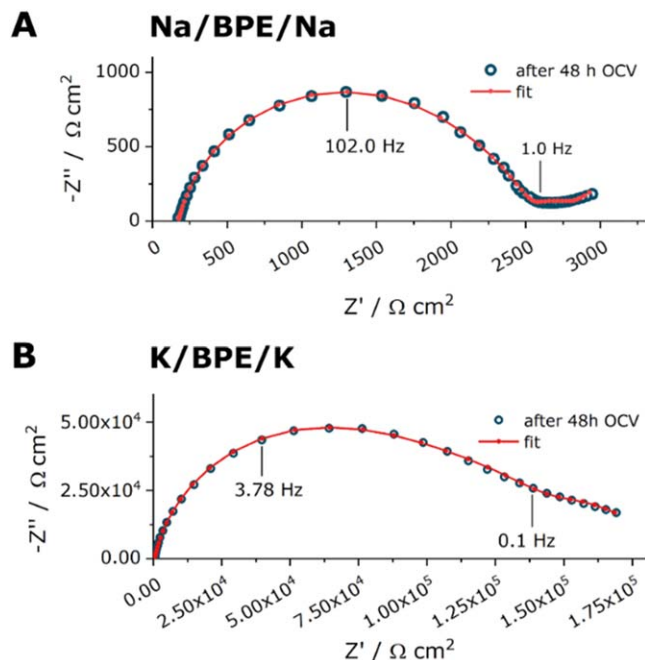
Figure 6. Nyquist plots of selected impedance spectra during the OCV/conditioning phase (prior to cycling) and their corresponding simulated circuits for Na/BPE/Na (A) and K/BPE/K (B) symmetric cells.

disproportional to the values obtained for the corresponding Na-cell. One reason for the strong increase during storage may also be related to formation of more resistive components at the electrode-electrolyte interface. This includes for instance the rapid reaction of trace amounts of moisture or oxygen in the glovebox atmosphere, which can readily lead to thicker surface layers during the K-metal electrode preparation (as compared to Na). An interesting phenomenon is the evolution of the cell impedance between the cycling sequences (see next section), since a significant decrease of R2 and R3 are seen after the OCV sequence.

EIS of solid-electrolyte cells (between cycling sequences).—The trends in resistance and Warburg coefficients are opposite for Na- and K-cells. The values increase in case of Na/BPE/Na cells, as one would expect from continued surface layer growth due to reactions between electrolyte components and plated Na metal (increasing R2; Fig. 7A; Q1 remains within the same order of magnitude, Fig. S10). Higher values for R3 are also observed but most notable after the first two cycling sequences. As shown in Fig. 8A the measured impedance is highest after the second cycling sequence amongst. The overall decreasing impedance after the third sequence was unexpected, as higher current densities should lead to faster electrode aging. As for the OCV samples, spectra of the Na/BPE/Na cells showed the low-frequency tail. The spectrum after sequence #3 even showed a clearly discernible local minimum. The nested ECM (Fig. 5D) produced wave-like tails, as described above, that reproduces the feature with some deviation.

In contrast, K/BPE/K cells showed strongly decreasing impedance with each measurement after a cycling sequence (Fig. 8B), which is induced by a pronounced decrease of the surface layer resistance R2, as well as a gradual reduction of the charge-transfer resistance R3. While the spectrum after sequence #1 still showed about 4-times larger impedance than the corresponding Na-cells, the spectra already approached similar values after the second sequence and the impedance of the K-cell dropped even below that of a Na-cell (to about half the value) after the third sequence. This is also shown in the evolution of the fitting parameters in Figs. 7C & 7D. Despite the gradual change in impedance, K/BPE/K cells further displayed the onset of a second arc in the low-frequency range that is

fitted well with a FLW. For this reason, the contribution for the FSW was negligibly small ($Z_{FSW} \rightarrow 0$) in the simulated spectra for the cycled samples. The strong decrease is also seen in other fitting parameters, such as Q1 that increased in the first two samples by an order of magnitude from values in the 10^{-4} S·s$^\alpha$ cm^{-2} range to the 10^{-3} S·s$^\alpha$ cm^{-2} but decreased in the last sample to values in the low 10^{-5} S·s$^\alpha$ cm^{-2} range (note that α-values changed for the cycled samples between 0.80–0.86, Figs. S7b & S7e). In contrast, values for Q2 are found in a range of low 10^{-5} (Na) to high 10^{-6} S·s$^\alpha$ cm^{-2} that is common for double layer capacitances. Similarly, with onset of cycling the Warburg time constant (τ) increased (Figs. S7c & S7f). For Na-cells it was the time constant of the FSW element ($\tau(Z_{FSW})$), while for K-cells the time constant of the FLW element increased $\tau(Z_{FLW})$. Compared to the last OCV samples, the changes were observed primarily on the second and third cycling sequence, i.e. after at least 20 cycles.

It should be highlighted that the spectra were recorded after a relaxation phase and not dynamic. Hence, cycling at different current densities only had indirect effects on the measurement, e.g. by changes in surface chemistry and diffusion processes, but does not include effects such as polarization under different load that was determined during the calorimetric experiments.

EIS for liquid electrolyte cell (Na/LE/Na).—For further comparison, a liquid electrolyte Na/Na cell at 55 °C was studied as well. Cell cycling of K/K symmetric cells with liquid electrolyte at 55 °C repeatedly failed and therefore no EIS spectra could be obtained. The Nyquist plots in Fig. 9A show the impedance after each of the three cycling sequences. In general, the impedance of the Na/LE/Na cell is a factor 10 smaller than for the corresponding solid electrolyte cell (Na/BPE/Na). It is also seen that the cell impedance is largest for the spectra recorded after the first cycling sequence and decreases continuously thereafter.

The model presented Fig. 5D is also a good fit for the analysis of the liquid electrolyte cell with one simplification: in the absence of a high frequency semicircle from the geometric capacitance C1, the RC circuit of the bulk electrolyte was reduced to a single resistor R1 (Fig. 9B). As shown in the evolution of the resistance parameters in Fig. 9C the largest change is seen for R2, which decreases from around 725 Ω cm^{-2} to 415 Ω cm^{-2}. R3 decreases from the first to the second sequence in a range between 150–200 Ω cm^{-2}. This behaviour was already observed for the solid electrolyte cells (Fig. 8) and seems to contradict the theory of growing surface layers at first glance (further discussed below). The parameters for the two constant phase elements are comparable to the ones observed in the solid electrolyte system (Fig. S10A). The analysis also showed the relevance of Z_{Ws} in simulating the region below 102 Hz (values of Warburg coefficients shown in Fig. 9D). The results of the simulated spectra (red lines) in Fig. 9A, suggests that even though the local minimum in the low-frequency transition around 200 mHz can be modelled with its minimum, discrepancies in the values of –Z' and in the low frequency tail were unavoidable in this model, unless the alpha-value is not restricted (limited to $0.40 < \alpha < 0.55$; ideally at 0.5 to describe the 45° TML, Fig. S10E). As pointed out by Moškon et al.[25] the dependencies in this region are quite complex when described in detail. Therefore, using Warburg elements can only be a practical approximation.

Alternative circuits.—In the above sections we provided a detailed analysis of the EIS data obtained during OCV storage after cell assembly and three different sequences of stripping and plating cycles. The basis for our analysis was the nested circuit proposed in Fig. 5D. Given the ambiguity of different equivalent circuits on the systems response, it can be challenging to correlate features in impedance spectra to system parameters with confidence. This is especially true if the ECM is not derived from physics-based models. To put the suggested nested circuit to a final test, the analysis was repeated on two spectra (one OCV, one after sequence 1) of the Na/BPE/Na cell (Figs. 10A and 10B). For this,
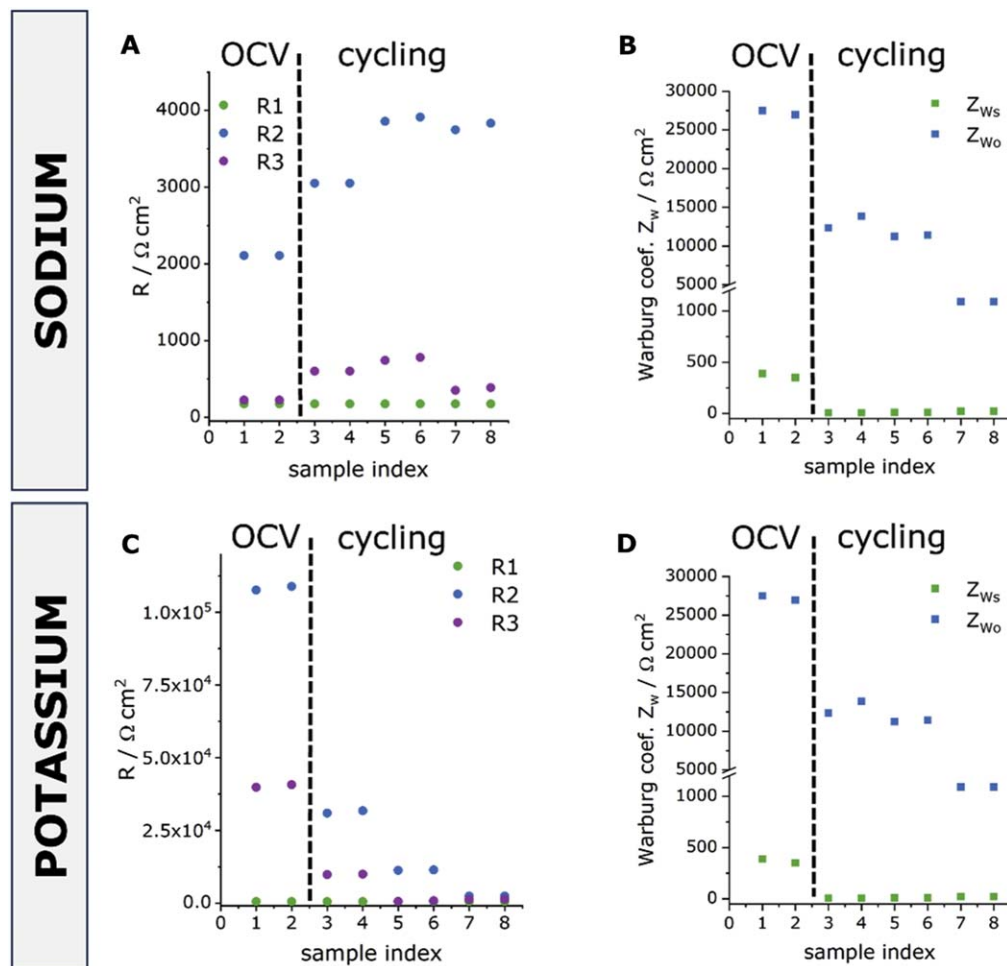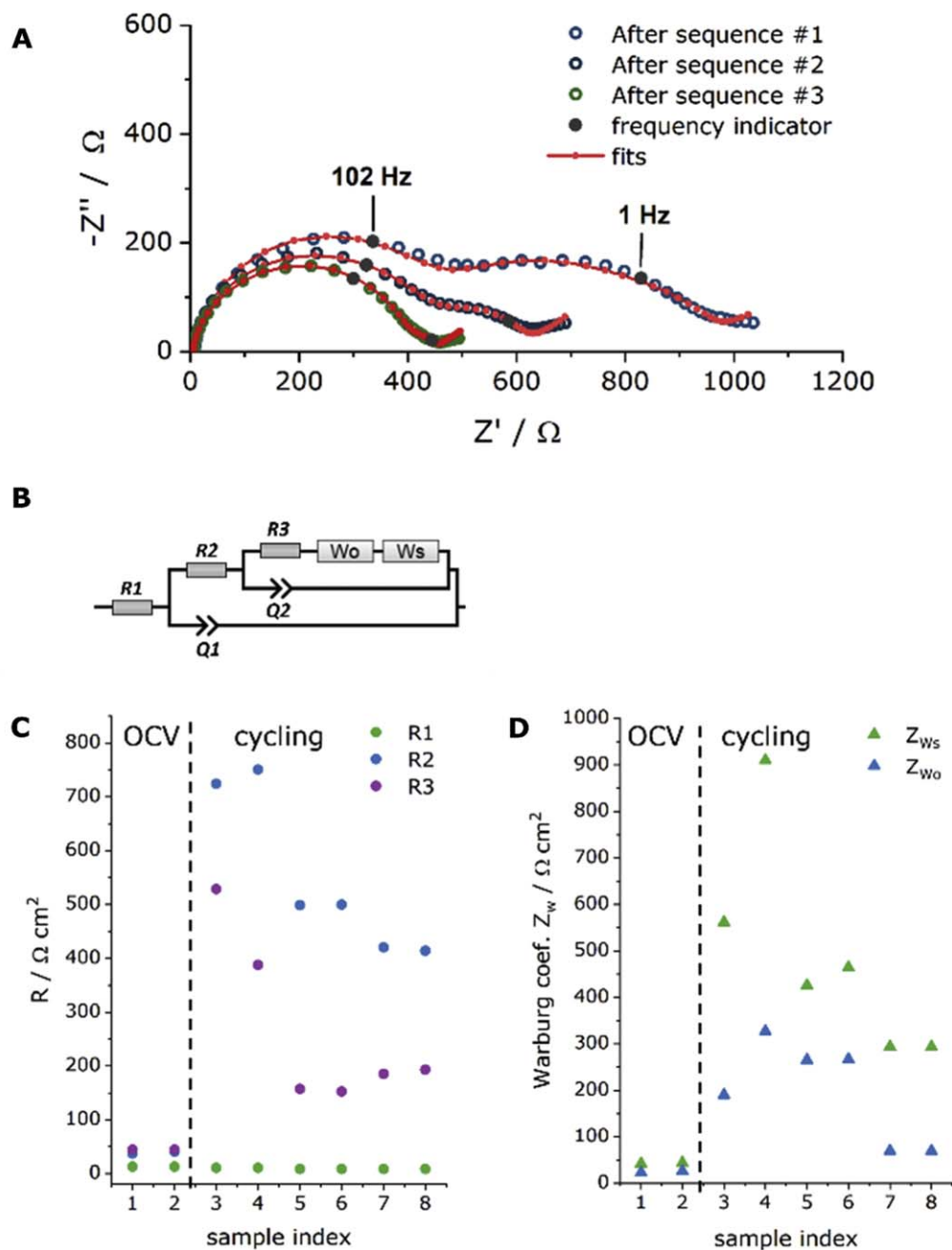
Figure 7. Fitting parameters of simulated circuits after 48 h at OCV (but prior to cycling; samples 1 & 2) and after each cycling sequence (left and right side of dotted line, respectively) for Na/BPE/Na (top row) and K/BPE/K (bottom row) cells. A and C show the fitted values for resistors R1, R2 and R3 and B and D show the Warburg resistances for Z_{Ws} and Z_{Wo}.
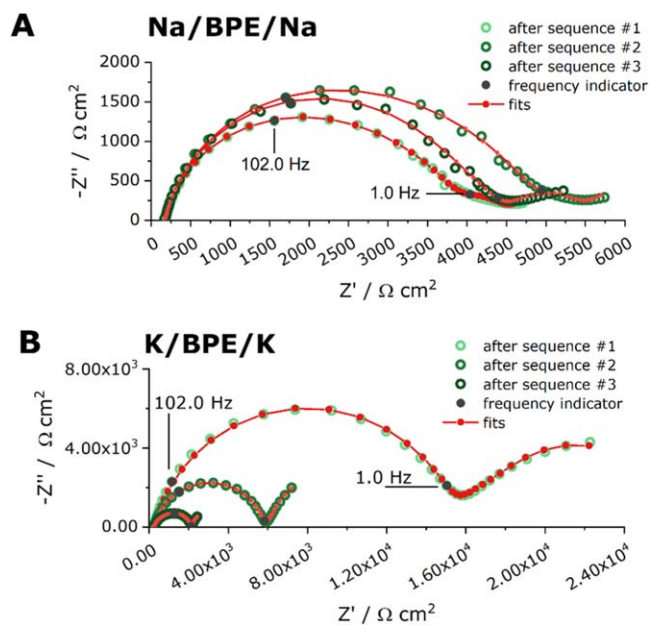
Figure 8. Nyquist plots of impedance spectra recorded after each cycling sequence (10 cycles at the same current density) and their corresponding simulated circuits for Na/BPE/Na (A) and K/BPE/K (B) symmetric cells.

two "arbitrary"-type equivalent circuits were chosen that are a series of Voigt elements (Fig. 10C). The first model (Serial-1) was terminated with a FLW. In the second model (Serial-2) FSW and FLW were included in the last RQ circuit, as charge-transfer and mass transport should be coupled. The first Voigt element was an RC circuit, to describe the electrolyte resistance (see above). In the other two cases C was replaced by CPEs, Q. The RC element related to the solid electrolyte is essentially independent from the rest of the circuit and does not need to be further considered. This was also noted during the work on the nested circuit above that the electrolyte RC can be in series (or nested) with the rest without affecting any other part of the fit. The Serial-1 and Serial-2 circuits deliver good results both in the Nyquist and the Bode plot (phase angle) in the high- and mid-frequency region. More importantly, the parameters R2, R3 and Z_{FLW} are generally in the same range as for the nested circuit (Fig. 10D). However, from the Serial-2 model the magnitudes of R2 and R3 are opposite to the other two models. Attempts to reverse the order yielded in unsatisfactory agreements between data and simulated circuit. Also, model Serial-2, yielded unreasonable low-frequency responses for any non-negligible parameter for Z_{FSW}. The fitting parameters for the capacitances, alpha exponent and the Warburg time constant are provided in Fig. S11). Especially Q1, spreads over 3 order of magnitude, depending on the model. Overall, the low-frequency response in both models, Serial-1 and −2, where the diffusion elements make an impact, was in poorer agreement with the data than the nested circuit model used above, as can be clearly seen in the Nyquist and Bode plot. On the other hand, if information from diffusion elements are not of

Figure 9. (A) Nyquist plots of impedance spectra recorded after each cycling sequence (10 cycles at the same current density) and their corresponding simulated circuits for the Na/LE/Na symmetric cell. (B) Equivalent circuit model. Fitting parameters are shown for resistances R1, R2 and R3 (C) as well as Warburg coefficients (D).

interest, such models can at least indicate magnitudes for the interfacial resistance, R2, and charge-transfer resistance, R3, which are extracted from the high- and mid-frequency range. Our analysis also showed that there is a risk that additional processes could be easily overlooked when the α exponent of the CPEs, Q, approach physically meaningless values if not restricted properly (here between 0.8–1), resulting in strongly depressed semicircles from the RQ response.

Discussion—Degradation at the polymer electrolyte/alkali metal interface.—As demonstrated above, the interpretation of impedance spectra on solid polymer electrolyte systems, can be particularly challenging as a result of the low ionic conductivity, even at elevated

temperatures. We found, by comparison to a liquid electrolyte cell (Na/Na), that the mid-frequency range is obscured by a large resistance contribution (R2) that is commonly assigned to the SEI layer. Interestingly, after a couple of cycles the resistances R3, assigned to the charge-transfer process, of both the liquid and solid electrolyte cells approached similar values in the range of a few hundred Ω cm^{-2}.

As the term "SEI" suggests, ion conduction in this interphase is thought to proceed along grain boundaries or the bulk of the particles formed during degradation reactions.[54] Judging from the magnitude of the obtained capacitances Q1 of the LE and BPE Na/Na cells (in the order of 10^{-4}, Figs. S7 and S10), the SEI layer thicknesses d should be similar, following Eq. 7,[64]
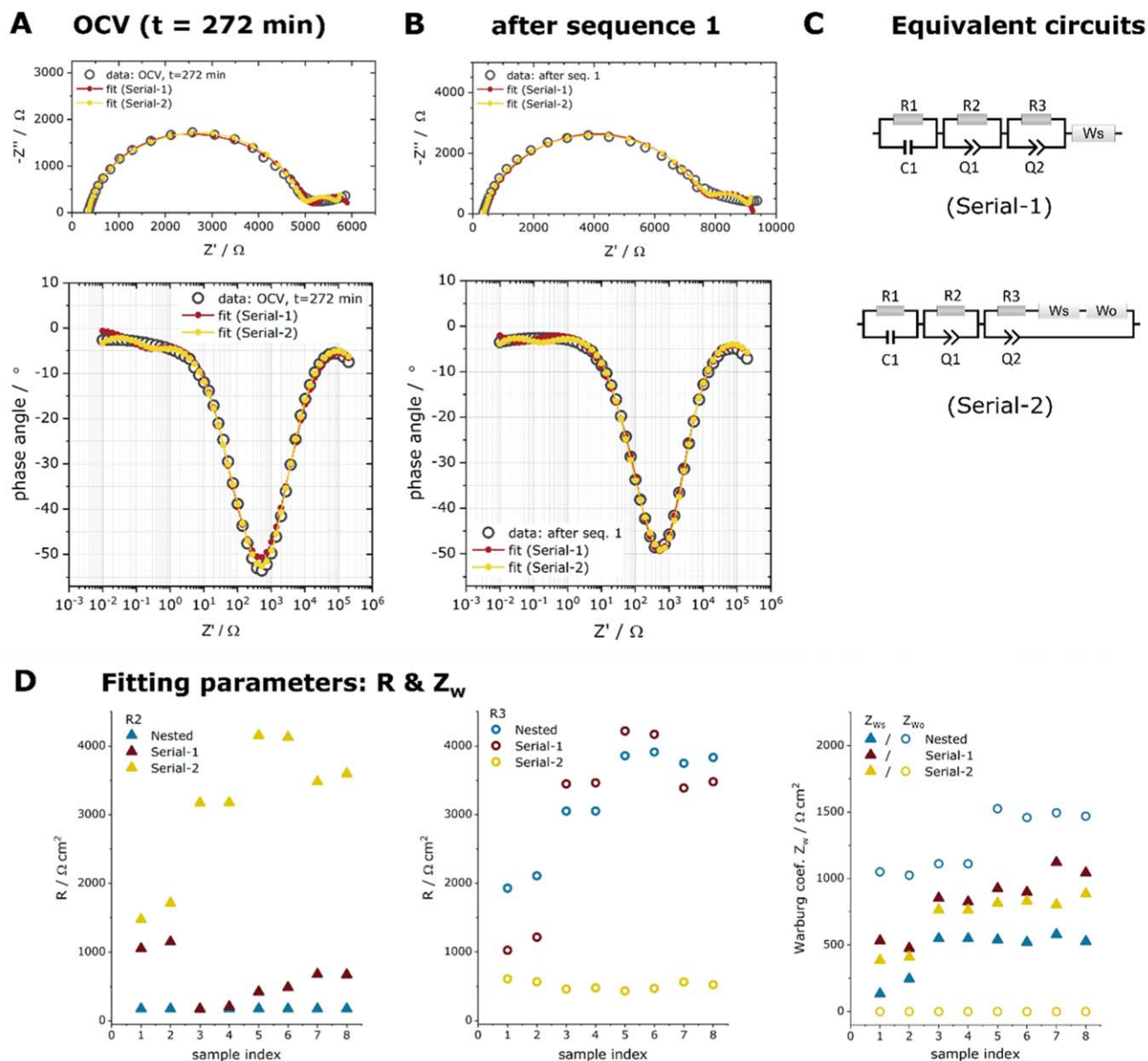
Figure 10. Comparison of different ECM for the Na/BPE/Na cell at OCV (prior to cycling, (A) and after the first cycling sequence (B). (C) equivalent circuits constructed from a series of Voigt elements; (D) Fitting parameters of the resistances R2 and R3, as well as the two Warburg coefficients Z_{Ws} and Z_{Wo}.

$$d = \frac{\varepsilon_0 \varepsilon_r \cdot A}{C} \qquad [7]$$

where A is the electrode area, C the capacitance (not Q), ε_0 the dielectric constants in vacuum and ε_r the specific dielectric constant (~5 for SEI components[65]). Post-mortem XPS studies on Li/SPE/Li cells further suggested that the SEI components formed in PEO-based SPE are surprisingly similar[12,13] to those formed in carbonate-based LE, although different relative proportions of the compounds are found.

With IMC experiment on the liquid carbonate-based electrolyte, the most frequently used electrolyte solvent system was investigate. However, carbonates display some differences in their SEI formation to (poly)ethers, which is a subject in future studies. The parasitic heat flow determined by IMC measurements (Fig. 4) showed higher values for BPE-based K-cells than for corresponding Na-cells, as expected from the reactivity series Li < Na < K. Under different current densities, the gradually increasing heat flow is almost exclusively attributed to higher ohmic resistances from the relatively low ionic conductivity of the SPEs. Compared to LE-cells, which showed a strong correlation between parasitic heat flow and current density, BPE-based systems displayed constant parasitic heat flows within margins. At the beginning of a new cycling sequence, the heat flow was generally higher than at the end of the sequence, which could suggest that more plated/stripped material leads initially to more parasitic reactions. Upon further cycling deposition occurs in the existing morphology which reduces the exposure of metallic deposits to the electrolyte.[66–68] Moreover, except for the cycling sequence at 10 μA cm^{-2} the specific heat was similar (20 μA cm^{-2}) or even smaller (50 μA cm^{-2}) than for the LE system.

However, the SEI layer formed in the BPE system likely comprises of solid SEI degradation products in an interpenetrated polymer matrix as the dominant ion-conducting phase. In contrast, for liquid electrolytes the SEI is infiltrated with a liquid phase with better transport properties.[52] The general decrease of R2 with increasing number of cycles is probably two-fold: (1) increase in electrode surface area through growth of a porous structure[50] (the

areal resistance herein was referred to geometric electrode area), (2) increasing SEI layer porosity[52] (particularly relevant for recurrent electrolyte degradation in liquid electrolytes when degradation products are soluble[60,69]) and (3) new alkali metal deposits in the interphase region that exhibit thinner, i.e. less resistive, surface layers initially.

In case of K-cells, repeated EIS measurements during the OCV/storage phase suggests the build-up of an increasingly resistive surface layer (10-fold larger than for the corresponding Na/BPE/Na cell), indicating considerable chemical changes (as no current is applied) at the K-metal surface during storage. Interestingly, after the first cycling sequence the high cell impedance almost disappeared completely and dropped even below that of the Na-cell, indicated by a considerable drop in R2 after the first cycling sequence. This suggests that the surface layer during OCV has different properties and is not as blocking (or resistive) than one would anticipate from the magnitude of R2. As a possible origin K-metal might exhibit markedly different surface species initially, i.e. after cell assembly in a glovebox atmosphere,[70] than after a few plating/stripping cycles. As the layer undergoes significant changes during electrodeposition and -dissolution, it is rendered more permeable to ions over time. To understand the underlying processes and surface layer evolution in more detail further studies will be required.

In summary, in this work it can be concluded that the K/BPE interface is highly dynamic, which might also be due to the high surface diffusivity of K on K-metal and the facile formation of mossy and dendritic morphologies already at low current densities.[70,71] Increases in electrochemical active surface area (EASA) from continued changes in surface morphology also explain the trend in decreasing resistances with increasing number of cycles and gradually increased current densities.[50] Unlike liquid electrolytes, the solubility of electrolyte components and the resulting recurrent SEI formation is reduced, which is also highlighted by the calorimetric results at higher current densities. Additional contributions to the impedance can arise when concentration gradients form in the electrolyte, which is seen in the low-frequency region. For LE this is a comparatively minor problem as compared to SPE. As we have demonstrated the combination of FSW and FLW allowed in most cases satisfactory goodness of fit. For a better reproduction, especially of the low-frequency region, more advanced TLM are likely more appropriate but not as straightforward to use.

Conclusions

In this work the reactivity of alkali metals towards solid polymer electrolytes (SPE) and carbonate-based liquid electrolytes was studied at elevated temperature of 55 °C by a combination of electrochemical impedance spectroscopy (EIS) and isothermal microcalorimetry (IMC). The results not only highlight the differences in reactivity of the alkali metals towards different electrolytes, but also, from a methodical perspective, the importance of separating heat contributions in IMC analysis as a powerful tool to study and quantify degradation processes in solid electrolyte systems in a non-invasive manner. As a key finding, IMC measurements could show that a continuous but constant degradation process is taking place in SPE-based cells, while the liquid electrolyte system showed strong dependencies to the applied current density.

For the analysis of the ac impedance data a nested ECM was suggested that uses a combination of two Warburg elements to reproduce the low-frequency features of the spectra. Key observations include experimental evidence for significant morphological changes and an associated increase in electrochemical active surface area in course of repeated stripping/plating processes. Further, the results demonstrated the strong dependence of EIS measurements on the storage and cycling history of Na- and K-cells. Especially K/BPE/K cells displayed significant changes between the initial OCV and cycling intervals. The impedance drifts pose additional challenges for example in the reproducible determination of transference numbers.[16,72] For better visualization of morphological changes at the electrode-electrolyte interface future studies can benefit from combining EIS or IMC with additional in situ and operando techniques, such as X-ray tomography or optical microscopy.

Data Availability Statement

The data that supports the findings of this study are available in the supplementary material of this article and are available from the corresponding author upon reasonable request.

ORCID

Ulf-Christian Rauska https://orcid.org/0000-0002-7450-8590
Fabian Jeschull https://orcid.org/0000-0002-5927-1978

References

1. H. Huo and J. Janek, *Natl Sci. Rev.*, **10**, 4 (2023).
2. J. T. Frith, M. J. Lacey, and U. Ulissi, *Nat. Commun.*, **14**, 420 (2023).
3. R. Weber, M. Genovese, A. J. Louli, S. Hames, C. Martin, I. G. Hill, and J. R. Dahn, *Nat. Energy*, **4**, 683 (2019).
4. D. Rehnlund, C. Ihrfors, J. Maibach, and L. Nyholm, *Mater. Today*, **21**, 1010 (2018).
5. J. Becherer, D. Kramer, and R. Mönig, *Chem. Electro. Chem*, **8**, 3882 (2021).
6. M. Srout, M. Carboni, J. Gonzalez, and S. Trabesinger, *Small*, **2206252**, 1 (2022).
7. S. Wenzel, T. Leichtweiss, D. Krüger, J. Sann, and J. Janek, *Solid State Ionics*, **278**, 98 (2015).
8. A. J. Butzelaar, P. Röring, T. P. Mach, M. Hoffmann, F. Jeschull, M. Wilhelm, M. Winter, G. Brunklaus, and P. Théato, *ACS Appl. Mater. Interfaces*, **13**, 39257 (2021).
9. U. Oteo, M. Martinez-Ibañez, I. Aldalur, E. Sanchez-Diez, J. Carrasco, M. Armand, and H. Zhang, *Chem. Electro. Chem*, **6**, 1019 (2019).
10. G. Hernández, I. L. Johansson, A. Mathew, C. Sångeland, D. Brandell, and J. Mindemark, *J. Electrochem. Soc.*, **168**, 100523 (2021).
11. L. Seidl, R. Grissa, L. Zhang, S. Trabesinger, and C. Battaglia, *Adv. Mater. Interfaces*, **9**, 2100704 (2022).
12. C. Xu, B. Sun, T. Gustafsson, K. Edström, D. Brandell, and M. Hahlin, *J. Mater. Chem. A*, **2**, 7256 (2014).
13. B. Sun, C. Xu, J. Mindemark, T. Gustafsson, K. Edström, and D. Brandell, *J. Mater. Chem. A*, **3**, 13994 (2015).
14. Y. Yusim, E. Trevisanello, R. Ruess, F. H. Richter, A. Mayer, D. Bresser, S. Passerini, J. Janek, and A. Henss, *Angew. Chemie - Int. Ed.*, **62** (2023).
15. E. E. Ushakova, A. Frolov, A. A. Reveguk, D. Y. Usachov, D. M. Itkis, and L. V. Yashina, *Appl. Surf. Sci.*, **589**, 153014 (2022).
16. A. D. Khudyshkina, A. J. Butzelaar, Y. Guo, M. Hoffmann, T. Bergfeldt, M. Schaller, S. Indris, M. Wilhelm, P. Théato, and F. Jeschull, *Electrochim. Acta*, **454**, 142421 (2023).
17. Y. Kobayashi, H. Miyashiro, K. Kumai, K. Takei, T. Iwahori, and I. Uchida, *J. Electrochem. Soc.*, **149**, A978 (2002).
18. W. Lu and J. Prakash, *J. Electrochem. Soc.*, **150**, A262 (2003).
19. B. Qin, M. Zarrabeitia, A. Hoefling, Z. Jusys, X. Liu, J. Tübke, R. J. Behm, G. Cui, A. Varzi, and S. Passerini, *J. Power Sources*, **560**, 232630 (2023).
20. L. E. Downie, S. R. Hyatt, and J. R. Dahn, *J. Electrochem. Soc.*, **163**, A35 (2016).
21. S. L. Glazier, L. E. Downie, J. Xia, A. J. Louli, and J. R. Dahn, *J. Electrochem. Soc.*, **163**, A2131 (2016).
22. S. L. Glazier, J. Li, A. J. Louli, J. P. Allen, and J. R. Dahn, *J. Electrochem. Soc.*, **164**, A3545 (2017).
23. S. Drvarič Talian, J. Moškon, R. Dominko, and M. Gaberšček, *Adv. Mater. Interfaces*, **9**, 2101116 (2022).
24. J. Moškon, J. Žuntar, S. Drvarič Talian, R. Dominko, and M. Gaberšček, *J. Electrochem. Soc.*, **167**, 140539 (2020).
25. J. Moškon and M. Gaberšček, *J. Power Sources Adv.*, **7**, 100047 (2021).
26. J. Moškon, S. Drvarič Talian, R. Dominko, and M. Gaberšček, *J. Electrochem. Sci. Eng.*, **10**, 79 (2020).

27. A. D. Khudyshkina, P. A. Morozova, A. J. Butzelaar, M. Hoffmann, M. Wilhelm, P. Theato, S. S. Fedotov, and F. Jeschull, *ACS Appl. Polym. Mater.*, **4**, 2734 (2022).
28. D. Bernardi, E. Pawlikowski, and J. Newman, *J. Electrochem. Soc.*, **132**, 5 (1985).
29. J. Asenbauer et al., *Adv. Sustain. Syst.*, **6**, 2200102 (2022).
30. F. Friedrich, T. Zünd, A. Hoefling, J. Tübke, and H. A. Gasteiger, *J. Electrochem. Soc.*, **169**, 040547 (2022).
31. L. Kraft, A. Hoefling, T. Zünd, A. Kunz, M. Steinhardt, J. Tübke, and A. Jossen, *J. Electrochem. Soc.*, **168**, 053505 (2021).
32. J. Asenbauer, A. Hoefling, S. Indris, J. Tübke, S. Passerini, and D. Bresser, *ACS Appl. Mater. Interfaces*, **12**, 8206 (2020).
33. B. Qin, T. Diemant, H. Zhang, A. Hoefling, R. J. Behm, J. Tübke, A. Varzi, and S. Passerini, *ChemSusChem*, **12**, 2609 (2019).
34. I. U. Mohsin, L. Schneider, M. Häringer, C. Ziebert, M. Rohde, W. Bauer, H. Ehrenberg, and H. J. Seifert, *J. Power Sources*, **545**, 231901 (2022).
35. S. Fang, L. Shen, A. Hoefling, Y. Wang, G. Kim, P. A. van Aken, X. Zhang, and S. Passerini, *Nano Energy*, **89**, 106421 (2021).
36. J. C. Burns, L. J. Krause, D.-B. Le, L. D. Jensen, A. J. Smith, D. Xiong, and J. R. Dahn, *J. Electrochem. Soc.*, **158**, A1417 (2011).
37. C. Erinmwingbovo, D. Koster, D. Brogioli, and F. La Mantia, *Chem. Electro. Chem*, **6**, 5387 (2019).
38. U. Krewer, F. Röder, E. Harinath, R. D. Braatz, B. Bedürftig, and R. Findeisen, *J. Electrochem. Soc.*, **165**, A3656 (2018).
39. B. Grysakowski, J. J. Jasielec, B. Wierzba, T. Sokalski, A. Lewenstam, and M. Danielewski, *J. Electroanal. Chem.*, **662**, 143 (2011).
40. M. Sluyters-Rehbach, *Pure Appl. Chem.*, **66**, 1831 (1994).
41. J. R. Macdonald, *Electrochim. Acta*, **35**, 1483 (1990).
42. R. De Levie, *Electrochim. Acta*, **8**, 751 (1963).
43. J. Landesfeind, J. Hattendorff, A. Ehrl, W. A. Wall, and H. A. Gasteiger, *J. Electrochem. Soc.*, **163**, A1373 (2016).
44. A. C. Lazanas and M. I. Prodromidis, *ACS Meas. Sci. Au*, **3**, 162 (2023).
45. J. Bisquert, *Phys. Chem. Chem. Phys.*, **2**, 4185 (2000).
46. Z. Siroma, N. Fujiwara, S. I. Yamazaki, M. Asahi, T. Nagai, and T. Ioroi, *Electrochim. Acta*, **160**, 313 (2015).
47. M. Adamič, S. D. Talian, A. R. Sinigoj, I. Humar, J. Moškon, and M. Gaberšček, *J. Electrochem. Soc.*, **166**, A5045 (2019).
48. U. Oteo, M. Martinez-Ibañez, I. Aldalur, E. Sanchez-Diez, J. Carrasco, M. Armand, and H. Zhang, *ChemElectroChem*, **6**, 1019 (2019).
49. S. J. Cooper, A. Bertei, D. P. Finegan, and N. P. Brandon, *Electrochim. Acta*, **251**, 681 (2017).
50. S. Drvarič Talian, J. Bobnar, A. R. Sinigoj, I. Humar, and M. Gaberšček, *J. Phys. Chem. C*, **123**, 27997 (2019).
51. J.-M. Atebamba, J. Moskon, S. Pejovnik, and M. Gaberšček, *J. Electrochem. Soc.*, **157**, A1218 (2010).
52. K. Lim, B. Fenk, J. Popovic, and J. Maier, *ACS Appl. Mater. Interfaces*, **13**, 51767 (2021).
53. V. Vivier and M. E. Orazem, "Impedance Analysis of Electrochemical Systems." *Chemical Reviews*, **122**, 11131 (2022).
54. M. Hess, *Electrochim. Acta*, **244**, 69 (2017).
55. T. Hosaka, S. Muratsubaki, K. Kubota, H. Onuma, and S. Komaba, *J. Phys. Chem. Lett.*, **10**, 3296 (2019).
56. W. Zhang, W. K. Pang, V. Sencadas, and Z. Guo, *Joule*, **2**, 1534 (2018).
57. K. N. Wood, M. Noked, and N. P. Dasgupta, *ACS Energy Lett.*, **2**, 664 (2017).
58. Z. Geng, Y. C. Chien, M. J. Lacey, T. Thiringer, and D. Brandell, *Electrochim. Acta*, **404**, 139727 (2022).
59. Z. Geng, S. Wang, M. J. Lacey, D. Brandell, and T. Thiringer, *Electrochim. Acta*, **372**, 137829 (2021).
60. A. Hofmann, F. Müller, S. Schöner, and F. Jeschull, *Batter. Supercaps*, **6**, e20230032 (2023).
61. C. Sångeland, G. Hernández, D. Brandell, R. Younesi, M. Hahlin, and J. Mindemark, *ACS Appl. Mater. Interfaces*, **14**, 28716 (2022).
62. J. Mindemark, M. J. Lacey, T. Bowden, and D. Brandell, *Prog. Polym. Sci.*, **81**, 114 (2018).
63. P. G. Kitz, M. J. Lacey, P. Novák, and E. J. Berg, *J. Power Sources*, **477**, 0 (2020).
64. A. Zaban and D. Aurbach, *J. Power Sources*, **54**, 289 (1995).
65. A. Zaban, E. Zinigrad, and D. Aurbach, *J. Phys. Chem.*, **100**, 3089 (1996).
66. B. Aktekin, L. M. Riegger, S. K. Otto, T. Fuchs, A. Henss, and J. Janek, *Nat. Commun.*, **14**, 6946 (2023).
67. C. Fang et al., *Nature*, **572**, 511 (2019).
68. F. Shi, A. Pei, D. T. Boyle, J. Xie, X. Yu, X. Zhang, and Y. Cui, *Proc. Natl. Acad. Sci. U. S. A.*, **115**, 8529 (2018).
69. R. Mogensen, D. Brandell, and R. Younesi, *ACS Energy Lett.*, **1**, 1173 (2016).
70. J. Popovic, *J. Electrochem. Soc.*, **169**, 030510 (2022).
71. P. Hundekar et al., *Proc. Natl Acad. Sci.*, **117**, 5588 (2020).
72. J. Serra Moreno, M. Armand, M. B. Berman, S. G. Greenbaum, B. Scrosati, and S. Panero, *J. Power Sources*, **248**, 695 (2014).